

# Hyperspectral polarimetric imaging of the ocean surface

CARLOS CARRIZO<sup>1</sup>, ANDRII GOLOVIN<sup>1</sup>, AHMED EL-HABASHI<sup>1</sup>, ROBERT FOSTER<sup>2</sup>, ALEXANDER GILERSON<sup>1</sup>

<sup>1</sup> The City College of New York, CUNY, New York, NY 10031, USA

<sup>2</sup> Remote Sensing Division, Naval Research Laboratory, Washington, DC 20375, USA

## Abstract

Hyperspectral imaging of the ocean is usually carried out by sensors on moving platforms, aircrafts or satellites, and is associated with scanning procedures for the acquisition of 3-D data cubes (along-track, cross-track and spectral). We present a state-of-the-art snapshot hyperspectral imager which simultaneously acquires spectra with 4nm spectral resolution in the wavelength range of 450-950nm with a 40 degree field-of-view (FOV). In addition, a computer controlled filter wheel installed in front of the imager allows for division-of-time Stokes vector image acquisition of the ocean surface.

Results are presented from several sets of measurements from ocean platforms in the NYC area, Duck, NC and from shipborne observations along the Florida coast. Measurements made by the imager are compared with simulations using a vector radiative transfer (VRT) code showing good agreement. Analysis of pixel-to-pixel variability of the total above water radiance ( $L_t$ ), sky radiance ( $L_s$ ) and derived water-leaving radiance ( $L_w$ ) for the viewing angles of 20-60 degrees in different wind conditions led to the estimation of uncertainties in measurements of these radiances in un-polarized and polarized modes for the whole spectral range and provide possible explanation of poor satellite retrievals in the blue bands in coastal waters.

## 1. Introduction

In ocean color (OC) applications, the accuracy of retrievals of water parameters depends on the quality of the estimated remote sensing reflectance,  $R_{rs}$ . One of the significant uncertainties in this estimation is associated with the characterization of the ocean surface, especially in windy conditions, and removal of the sky component reflected from this surface [1-3]. The impact of the wind-roughened surface on the radiance is estimated based on statistics of Cox and Munk (CMS) [4], who measured wave slopes as a function of the wind speed. Typically, for *in-situ* OC measurements, Cox-Munk statistics (derived from an approximate wind speed measurement) are the only available indicator of the instantaneous sea state. The reflectance coefficient of skylight from the sea surface,  $\rho$ , depends strongly on knowledge of the sea state, but also significantly on wavelength, aerosol characteristics and polarization effects, which are not routinely measured [2, 5-9].

Basic design of the hyperspectral push-broom imagers requires the motion of the platform, a rotatable mirror or similar scanning technique. Recent development of “snapshot” hyperspectral imagers eliminates this difficulty, and while such instruments have their own disadvantages, measurements can be made from non-moving platforms, ships, etc., providing an abundance of new data and capabilities [10] including estimations of variability in radiances induced by fluctuations of the wind-driven water surface.

The goal of this extended abstract is to demonstrate the capabilities of a new snapshot hyperspectral imager for applications of interest to the OC community, including characterization of the ocean surface, estimation of the uncertainties associated with above water radiometric measurements and derived water leaving radiances ( $L_w$ ), comparison of these results with radiative transfer simulations and removal of the sky component reflected from this surface.

## 2. Background

Cox-Munk statistics (CMS) are included in multiple scalar [11] and vector [5, 12-16] radiative transfer (VRT) models and allows simulation of the mean radiance spectra for differing wind speeds and various atmospheric and water conditions. However, these simulations do not estimate the uncertainties in measurements of the water in windy conditions. Several factors drive these uncertainties, and in this work they will be evaluated using a robust snapshot hyperspectral imager.

A snapshot hyperspectral imager UHD285 (Cubert GmbH, Germany), shown in Fig. 1d, was used in field measurements of ocean waters from several stationary platforms and from ships. The instrument is capable of acquiring 20 cubes/s of hyperspectral data in the visible/NIR part of the spectrum (i.e. 450-1000nm), 4 nm spectral sampling, and 14-bit digitization within a 40° field of view (FOV). The imager provides spectra for 50x50 pixels and a high spatial resolution panchromatic image (i.e. 1000x1000). The imager was further modified to acquire polarized data cubes by installation of a carousel 5-filter wheel in front of the imager to automatically collect one dark measurement, one unpolarized image and three polarized images with linear glass polarizers oriented at 0°, 90°, and 45° with respect to a reference axis. The instrument was calibrated in polarized and unpolarized mode by comparison of the radiance from the white plaque spectrum, which was simultaneously measured by GER 1500 spectroradiometer (SpectraVista, NY).

## 3. Approach

Above water observations were carried out from three stationary coastal platforms and one shipborne cruise: a) a 150-m long platform located in Brooklyn, NY; b) an offshore platform located 2 miles offshore from Northport, NY, c) a 500-m long pier located in Duck, NC, and d) aboard a NOAA research vessel (i.e. Okeanos Explorer) which travelled into the Gulf of Mexico and around the Florida coast.

The imager was installed on a tripod and oriented at 40° from nadir for the observations of the water surface ( $L_t$ ) and at 40° from zenith for sky observations ( $L_s$ ). The relative solar azimuth angle was fixed at  $\pm 90^\circ$ . The imager's 40° FOV covered the range of viewing angles (VA) from 20° to 60° with respect to nadir (water-viewing) and zenith (sky-viewing). Accompanying the imager's measurements, Inherent Optical Properties (IOPs) of water were measured in-situ using an ac-s instrument (WET Labs, OR) during the measurements at Duck, NC and ship cruise. For the Pier in NY, water samples were collected and then measured in the CCNY laboratory using the same instrument. Wind speed was measured by a handheld anemometer at NY sites and by permanently installed anemometers at Duck and during ship cruise. In addition, co-located and simultaneous measurements were acquired using a handheld GER instrument, which allowed further comparison with the imager. Aerosol optical thickness (AOT) was measured by a Microtops Sun-photometer.

Full description of the related theory and VRT simulations was previously given in details elsewhere [9-10], and it is briefly repeated here.

As mentioned before, the main parameter of interest in the field of OC used in the retrievals of water properties is the remote sensing reflectance  $R_{rs}$  [17]:

$$R_{rs}(\theta_v, \phi_v, \lambda) = L_w(\theta_v, \phi_v, \lambda) / E_d(\lambda) \quad (1)$$

where  $L_w(\theta_v, \phi_v, \lambda)$  is the water leaving radiance,  $E_d(\lambda)$  is the downwelling irradiance,  $\theta_v, \phi_v$  are the viewing (VA) and azimuth angles respectively and  $\lambda$  is the wavelength. VAs are

measured from nadir and the azimuth angle is equal to  $0^\circ$  when the Sun and the sensor are in opposition.

For above surface ocean observations, assuming that Sun glint is avoided and there are no whitecaps,  $L_w(\theta_v, \phi_v, \lambda)$  is determined from

$$L_t(\theta_v, \phi_v, \lambda) = L_w(\theta_v, \phi_v, \lambda) + \rho L_s(\pi - \theta_v, \phi_v, \lambda) \quad (2)$$

where  $L_t(\theta_v, \phi_v, \lambda)$  is the total upwelling radiance leaving the ocean surface, with a typical relative solar azimuth angle of  $\phi_v = 90^\circ$  or  $\phi_v = 135^\circ$  [18]. For a flat surface, the  $\rho$  coefficient is the Fresnel coefficient ( $\rho_F$ ) defined by the VA [19] and the indices of refraction of the air and water, but in the presence of ocean waves it is also a function of the illumination conditions and wind speed. For the illumination (solar) angle  $\theta_i = 40^\circ$ ,  $\phi_v = 90^\circ$  and  $\theta_v = 40^\circ$ ,  $\rho_F = 0.0256$ , while for a wind speed of  $W = 5\text{m/s}$ ,  $\rho = 0.028$  [18]. This last value of the coefficient is often used in the shipborne above water observations and is assumed to be independent of the wavelength for the whole range of 400-900 nm which are of interest for OC. However, a small dependence of  $\rho$  on the wavelength (about 5-10%) exists due to the dispersion of sea water [20]. It was shown that  $\rho$  is also affected by polarization, aerosol optical thickness (AOT) and aerosol scattering matrix [7-9, 21], as well as small amount of unavoidable Sun glint contamination in Zhang et al. [8].

In this work, the RayXP VRT code [15] was used in closure with the measurements from the imager. This code was successfully benchmarked against other VRT codes [15, 22] and polarimetric measurements of the atmosphere-ocean system [23-25] and surface effects [9]. The Stokes vectors corresponding to the radiance arriving at the sensor from the water body ( $L_t$ ) and the sky ( $L_s$ ) were computed from the simulations of the atmosphere-ocean system using auxiliary data (including IOPs and AOTs *in-situ* data). Isotropic Cox-Munk slope distributions [4] were assumed for all simulations based on average wind speed (W) measurements.

The full uncertainty equation for the total radiance (assuming 1-sigma uncertainties and lack of glint and foam, Eq. (2)) is given as [26]

$$\sigma_t^2 = \begin{bmatrix} \frac{\partial L_t}{\partial L_w} & \frac{\partial L_t}{\partial L_s} & \frac{\partial L_t}{\partial \rho} \end{bmatrix} \begin{bmatrix} \sigma_w^2 & \sigma_{ws} & \sigma_{w\rho} \\ \sigma_{ws} & \sigma_s^2 & \sigma_{s\rho} \\ \sigma_{w\rho} & \sigma_{s\rho} & \sigma_\rho^2 \end{bmatrix} \begin{bmatrix} \frac{\partial L_t}{\partial L_w} & \frac{\partial L_t}{\partial L_s} & \frac{\partial L_t}{\partial \rho} \end{bmatrix}^T \quad (3)$$

where all covariance terms are included. Using  $\frac{\partial L_t}{\partial L_w} = 1$ ,  $\frac{\partial L_t}{\partial L_s} = \rho$  and  $\frac{\partial L_t}{\partial \rho} = L_s$  this yields

$$\sigma_t^2 = \sigma_w^2 + \rho^2 \sigma_s^2 + L_s^2 \sigma_\rho^2 + 2\rho L_s \sigma_{s\rho} + 2\rho \sigma_{ws} + 2L_s \sigma_{w\rho} \quad (4a)$$

It is common practice in estimation of *in-situ*  $L_w$  to assume that  $\rho$  is almost constant (and  $\sigma_\rho$  is small or negligible). This is only a valid assumption under conditions of very low wind speed, low VA, and large solar zenith angles ( $\theta_i$ ) where the contribution of Sun glitter is small. The variance of the total water signal would then be

$$\sigma_t^2 \approx \sigma_w^2 + \rho^2 \sigma_s^2 + 2\rho \sigma_{ws} \quad (4b)$$

From the subtraction of Eq. (4b) from (4a), we can estimate the effect of the assumption as:

$$L_s^2 \sigma_\rho^2 + 2L_s \sigma_{w\rho} \approx 0 \text{ or } \sigma_\rho \approx -2r_{w\rho} \sigma_w / L_s \quad (4c)$$

where  $r_{w\rho}$  is the correlation coefficient for  $L_w$  and  $\rho$ . This allows establishing a relationship between parameters  $\sigma_\rho$  and  $\sigma_w$  in a preliminary manner. Similarly, using derivation in Eq. (3) and Eq. (2) in the form  $L_w = L_t - \rho L_s$ , yields

$$\sigma_w^2 \approx \sigma_t^2 + \rho^2 \sigma_s^2 - 2\rho \sigma_{ts} \text{ and } L_s^2 \sigma_\rho^2 \approx 2L_s \sigma_{t\rho} \text{ or } \sigma_\rho \approx 2r_{t\rho} \sigma_t / L_s \quad (5)$$

Using data from the imager in the form  $L_w + \delta_w = L_t + \delta_t - \rho(L_s + \delta_s)$ , where  $\delta_w$ ,  $\delta_t$  and  $\delta_s$  are radiance deviations from the mean for each pixel, we can quantify components  $\sigma_w$ ,  $\sigma_t$ ,  $\sigma_s$ ,  $\sigma_{ws}$ ,  $\sigma_{ts}$  as well as corresponding correlation coefficients in Eqs. (4) and (5) to estimate realistic uncertainties in measurements of these parameters and contributions to the total signals. However, uncertainties in  $\sigma_w$  under the assumption of constant  $\rho$  will reflect the uncertainty in the derivation of  $L_w$  and not necessarily the natural variations of  $L_w$ .

As a first approximation, if we consider the relationship  $\delta_\rho \approx 2r_{t\rho} \delta_t / L_s$  derived from the last expression in Eq. (5), and use data from the imager in the form  $L_w + \delta_w = L_t + \delta_t - (\rho + \delta_\rho)(L_s + \delta_s)$  where  $r_{t\rho}$  is the correlation coefficient for  $L_t$  and  $\rho$ , we can estimate a more realistic  $\sigma_w$  including fluctuations in  $\rho$  by means of  $\sigma_\rho$ .

Since  $\sigma_\rho$  cannot be determined from equations (4) and (5), we need to compute  $\sigma_\rho$  using CMS. The Gaussian probability density function describing the wave slopes is  $f(x | \sigma_{iso}^2) = \exp\left(\frac{-x^2}{2\sigma_{iso}^2}\right) (2\pi\sigma_{iso}^2)^{-1/2}$ , where  $\int_{-\infty}^{\infty} f(x) dx \equiv 1$  and  $\sigma_{iso}^2 = 0.003 + 0.00512W$ , the variance of the isotropic slope distribution [4].  $W$  is the wind speed,  $x$  is the wave slope and  $\rho_F$  the corresponding unpolarized Fresnel coefficient for the incidence angle resulting in reflection toward  $\theta_v$ .

$$\sigma_\rho^2(\theta_v, \sigma_{iso}^2) = \int_{-\infty}^{\infty} f(x) \rho_F^2 dx - \left( \int_{-\infty}^{\infty} f(x) \rho_F dx \right)^2 \quad (6)$$

With these relationships and other terms measured with the imager, the spectra of covariances  $\sigma_{w\rho}$  and  $\sigma_{t\rho}$  (and corresponding  $r_{w\rho}$  and  $r_{t\rho}$ ) were determined from Eqs. (4) and (5).

In addition to the pixel-by-pixel exploration of water ( $L_t$ ) and sky ( $L_s$ ) radiances to determine the uncertainties in  $L_w$ , radiance distributions can be used to explore the dependence of measured radiances on the FOV of the instrument. Radiances within the full-angle FOV ( $\theta_{FOV}$ ) up to 35° were calculated using the following expression:

$$L_{t,s}(\lambda) = \frac{1}{\Omega_{FOV}} \iint_{\Omega_{FOV}} L_t(\lambda) d\Omega_{FOV} \quad (7)$$

where  $\theta_f = 1/2\theta_{FOV}$ ,  $L_{t,s}$  is the radiance for  $L_t$  and  $L_s$  (respectively),  $\Omega_{FOV}$  is the solid angle corresponding to the conical FOV and  $L_t$  is the radiance for each individual pixel within the FOV.

Finally, in above water measurements, the mean value of the reflectance coefficient  $\rho$  depends on the wind speed, wavelength, AOT and polarization effects [9]. Thus the impact of the sky reflectance can be minimized if AOT is measured and spectral  $\rho$  calculated accordingly.

Alternatively the signal from the sky can be almost completely removed from  $L_t$ . This can be achieved by placing a vertically oriented linear polarizer in front of the imager, as recommended earlier in [1-2] and removing mostly horizontally polarized skylight reflected from the sea surface. It should be noted that Sun glint is polarized in the main plane and is not removed by the polarizer on the sensor installed at  $\phi_v = \pm 90^\circ$ .

## 4. Results

### 4.1 Radiance spatial distribution, estimation of uncertainties

The main advantage of the imager is the availability of the radiance spatial distribution over the FOV for each wavelength. An example of such data for three wavelengths for  $L_t$ ,  $L_s$  and derived by Eq. (2)  $L_w$  is shown in Fig. 1a demonstrating radiance variability and opening the possibility for the statistical analysis of the radiance fluctuations spectrally and for various viewing and azimuth angles. Corresponding panchromatic water and sky images are shown at the bottom of Fig. 1 including the imager set-up at a stationary platform (i.e. installed on top of a tripod). It should be noticed that coordinates  $\theta_v$  and  $\phi_v$  are shown for the center of the image; small differences in the scales at the different parts of the image were not taken into account. Examples of spectra measured at four stations (two in open-ocean and two in coastal waters) for different VAs are shown in Fig. 2 with comparison with GER at  $40^\circ$ .

Measured spectra for the whole range of viewing angles  $20-60^\circ$  were compared with VRT simulations for measurements at the Duck, NC platform and wind speed of 5.6m/s. In such matchups mean spectra in the regions of interests (ROIs) corresponding to different VA as shown in Fig. 3a and 3b, and their simulated counterparts were compared. Pixel-by-pixel estimation of water leaving radiance using Eq. (2) is shown in Fig. 3c. VRT simulations were performed using RayXP program [15] and data cubes were produced, matching the spectral and spatial resolution of the imager ( $50 \times 50 \times 113$ ). For this study we limited the wavelength range to 450-900nm.

For all stations studied standard deviations  $\sigma_t$  and  $\sigma_s$  for the water and sky data and corresponding ratios  $\sigma_t/L_t$  and  $\sigma_s/L_s$  for each viewing angle were calculated over the imager's FOV with example for the case with wind speed  $W = 5.6$  m/s shown in Fig. 3d. All values were calculated based on the ROIs' configuration shown in Fig. 3a and 3b.

The contribution of different components in Eqs. (4) and (5) were evaluated and led to the coefficient of variation (CV)  $\sigma_w/L_w$  as a function of wind speed for all stations as shown in Fig. 4. The CV is in the range of 3-8% for most VAs with increase to 6-20% in the NIR and typically larger values for VA =  $60^\circ$ .

Although the imager is unable to acquire data  $<450$ nm, it is expected that since  $L_s$  does not change significantly in 400-450nm compared to 450nm and  $\sigma_w$  is mostly determined by  $\sigma_p L_s$ ,  $\sigma_w$  will remain approximately the same.  $L_w$  remains high in the blue in the open ocean, so the retrievals of  $R_{rs}$  in the open ocean are relatively stable. In coastal areas with very low  $L_w$  in the blue, the uncertainty in  $R_{rs}$  becomes much higher, thus explaining poor satellite retrievals in coastal waters.

#### **4.2 Field of view considerations in above water measurements**

Example of the spectra for different FOVs is shown for  $W = 4.5\text{m/s}$  in Fig. 5 with the corresponding images and analyzed areas. Statistics are presented only for one water and one sky image, but results were similar for many stations with different conditions with most stable results for  $\theta_{FOV} > 3-4^\circ$ .

#### **4.3 Measurements of water leaving radiance with vertical polarizer**

As it can be seen in Fig. 6, vertical polarizer practically eliminates sky component for all viewing angles in the studied range. The difference between the unpolarized signal and the one passing through the vertical polarizer (after dividing it by the transmittance of the polarizer,  $\tau_{POL}$ ) is very similar to the signal of the sky multiplied by the surface reflectance coefficient ( $\rho$ ) using CMS. There are still some spectral discrepancies that could be due to a combination of factors.

### **5. Conclusions**

A novel hyperspectral imager is introduced for OC applications in coastal waters and its advantages over non-imaging spectroradiometer and push broom imagers are discussed. The instrument provides hyperspectral radiance distribution with a wide FOV and short exposure time, which is valuable for the direct characterization of the wind-roughened surface in various illumination conditions and wind speeds. Comparison of the  $R_{rs}$  (Fig. 2) spectra from the imager and GER demonstrated very good consistency for all measurements confirming the high quality of the imager calibration.

Spectra of standard deviations for the radiance from the water and the sky at the viewing angles  $20-60^\circ$  are accurately determined and their ratios to the corresponding mean radiances are evaluated, showing that the coefficients of variation  $\sigma_i(\lambda)/L_i(\lambda)$  for water and  $\sigma_s(\lambda)/L_s(\lambda)$  for the sky measurements can be in the range of 3-20% depending on the viewing angle, wind speed and wavelength. The minimal values of  $\sigma_i(\lambda)/L_i(\lambda)$  are typically around viewing angle of  $40^\circ$ .

Different terms making up for the uncertainties in water leaving radiance ( $\sigma_w$ ) were explored using direct measurements from the snapshot imager and  $\sigma_w/L_w$  were determined. While it is not directly seen from the imager data with the minimum wavelength of 450 nm, it is expected that  $\sigma_w$  will be similar in 400-450nm range proportionally to weakly changing  $L_s$ , thus minimally affecting  $R_{rs}$  retrievals in the open ocean and more significantly  $R_{rs}$  retrievals in coastal waters with strongly decreasing  $L_w$ .

It is shown that for both  $L_i(\lambda)$  and  $L_s(\lambda)$  the impact of FOV is minimal, at least till  $W = 5.7\text{m/s}$  studied for FOV of  $4^\circ$  and larger.

It is demonstrated that vertical polarizer successfully eliminates sky contribution in a broad range of viewing angles.

### **Acknowledgments**

This work was supported by NASA Ocean Biology and Biochemistry Program, NOAA Cal/val program and the Office of Naval Research. This research was performed while Robert Foster held an NRC Research Associateship award at the U.S. Naval Research Laboratory in Washington, DC.

## References

1. J. L. Mueller, G. S. Fargion, and C. R. McClain, eds., "Ocean Optics Protocols for Satellite Ocean Color Sensor Validation, Revision 4, Volume III: Radiometric Measurements and Data Analysis Protocols," NASA/TM- 2003-211621 (2003).
2. B. Fougnie, R. Frouin, P. Lecomte, and P. Y. Deschamps, "Reduction of skylight reflection effects in the above water measurement of marine diffuse reflectance," *Appl. Opt.* **38**(18), 3844–3856 (1999).
3. N. A. Krotkov and A. P. Vasilkov, "Reduction of skylight reflection effects in the above-water measurement of diffuse marine reflectance: comment," *Appl. Opt.* **39**(9), 1379-1381, (2000).
4. C. Cox and W. Munk, "Measurement of the Roughness of the Sea Surface from Photographs of the Sun's Glitter," *J. Opt. Soc. Am.* **44**(11), 838–850 (1954).
5. C. D. Mobley, "Polarized reflectance and transmittance properties of windblown sea surfaces," *Appl. Opt.* **54**(15), 4828–4849 (2015).
6. Z. Lee, Y.-H. Ahn, C. Mobley, and R. Arnone, "Removal of surface-reflected light for the measurement of remote-sensing reflectance from an above-surface platform," *Opt. Express* **18**(25), 26313–26324 (2010).
7. R. Foster and A. Gilerson, "Polarized transfer functions of the ocean surface for above-surface determination of the vector submarine light field," *Appl. Opt.* **55**(33), 9476–9494 (2016).
8. X. Zhang, S. He, A. Shabani, P. W. Zhai, and K. Du, "Spectral sea surface reflectance of skylight," *Opt. Express* **25**(4), A1–A13 (2017).
9. A. Gilerson, C. Carrizo, R. Foster, T. Harmel, "Variability of the reflectance coefficient of skylight from the ocean surface and its implications to Ocean Color," *Optics Express*, **26**(8), 9615-9633 (2018).
10. C. Carrizo, A. Golovin, A. El-Habashi, R. Foster, D. Gray, J. Bowles, A. Gilerson, "Ocean surface characterization using snapshot hyperspectral polarimetric imager," *Proc. of SPIE* 10631 (2018).
11. C. D. Mobley, L. K. Sundman, HYDROLIGHT 4.2, Sequoia Scientific, Inc. (2001).
12. H. R. Gordon and M. Wang, "Retrieval of water-leaving radiance and aerosol optical thickness over the oceans with SeaWiFS: a preliminary algorithm," *Appl. Opt.* **33**(3), 443–452 (1994).
13. J. Chowdhary, B. Cairns, and L. D. Travis, "Contribution of water-leaving radiances to multiangle, multispectral polarimetric observations over the open ocean: bio-optical model results for case 1 waters," *Appl. Opt.* **45**(22), 5542–5567 (2006).
14. M. Chami, R. Santer, and E. Dilligeard, "Radiative transfer model for the computation of radiance and polarization in an ocean-atmosphere system: polarization properties of suspended matter for remote sensing," *Appl. Opt.* **40**(15), 2398–2416 (2001).
15. H. H. Tynes, G. W. Kattawar, E. P. Zege, I. L. Katsev, A. S. Prikhach, and L. I. Chaikovskaya, "Monte Carlo and multi-component approximation methods for vector radiative transfer by use of effective Mueller matrix calculations," *Appl. Opt.* **40**(3), 400–412 (2001).
16. P.-W. Zhai, Y. Hu, J. Chowdhary, C. R. Trepte, P. L. Lucker, and D. B. Josset, "A vector radiative transfer model for coupled atmosphere and ocean systems with a rough interface," *J. Quant. Spectrosc. Radiat. Transf.* **111**(7–8), 1025–1040 (2010).
17. C. D. Mobley, "Ocean Optics Web Book," <http://www.oceanopticsbook.info/>

18. C. D. Mobley, "Estimation of the remote-sensing reflectance from above-surface measurements," *Appl. Opt.* **38**(36), 7442–7455 (1999).
19. E. Hecht, *Optics* (Pearson Education, 2009).
20. X. Quan and E. S. Fry, "Empirical equation for the index of refraction of seawater," *Appl. Opt.* **34**(18), 3477–3480 (1995).
21. T. Harmel, A. Gilerson, A. Tonizzo, J. Chowdhary, A. Weidemann, R. Arnone, and S. Ahmed, "Polarization impacts on the water-leaving radiance retrieval from above-water radiometric measurements," *Appl. Opt.* **51**(35), 8324–8340 (2012).
22. A. Kokhanovsky, V. P. Budak, C. Cornet, M. Duan, C. Emde, I. L. Katsev, D. A. Klyukov, S. V. Korkin, L. CLabonnote, B. Mayer, Q. Min, T. Nakajima, Y. Ota, A. S. Prikhach, V. V. Rozanov, T. Yokota, and E. P. Zege, "Benchmark results in vector atmospheric radiative transfer," *J. Quant. Spectrosc. Radiat. Transf.* **111**(12–13), 1931–1946 (2010).
23. A. A. Gilerson, J. Stepinski, A. I. Ibrahim, Y. You, J. M. Sullivan, M. S. Twardowski, H. M. Dierssen, B. Russell, M. E. Cummings, P. Brady, S. A. Ahmed, and G. W. Kattawar, "Benthic effects on the polarization of light in shallow waters," *Appl. Opt.* **52**(36), 8685–8705 (2013).
24. P. C. Brady, A. A. Gilerson, G. W. Kattawar, J. M. Sullivan, M. S. Twardowski, H. M. Dierssen, M. Gao, K. Travis, R. I. Etheredge, A. Tonizzo, A. Ibrahim, C. Carrizo, Y. Gu, B. J. Russell, K. Mislinski, S. Zhao, and M. E. Cummings, "Open-ocean fish reveal an omnidirectional solution to camouflage in polarized environments," *Science* **350**(6263), 965–969 (2015).
25. M. Ottaviani, R. Foster, A. Gilerson, A. Ibrahim, C. Carrizo, A. El-Habashi, B. Cairns, J. Chowdhary, C. Hostetler, J. Hair, S. Burton, Y. Hu, M. Twardowski, N. Stockley, D. Gray, W. Slade, and I. Cetinic, "Airborne and shipborne polarimetric measurements over open ocean and coastal waters: intercomparisons and implications for spaceborne observations," *Remote Sens. Environ.* **206**, 375–390 (2018).
26. A. Bevan, "Statistical Data Analysis for the Physical Sciences," (Cambridge University Press, 2013).

## Figures

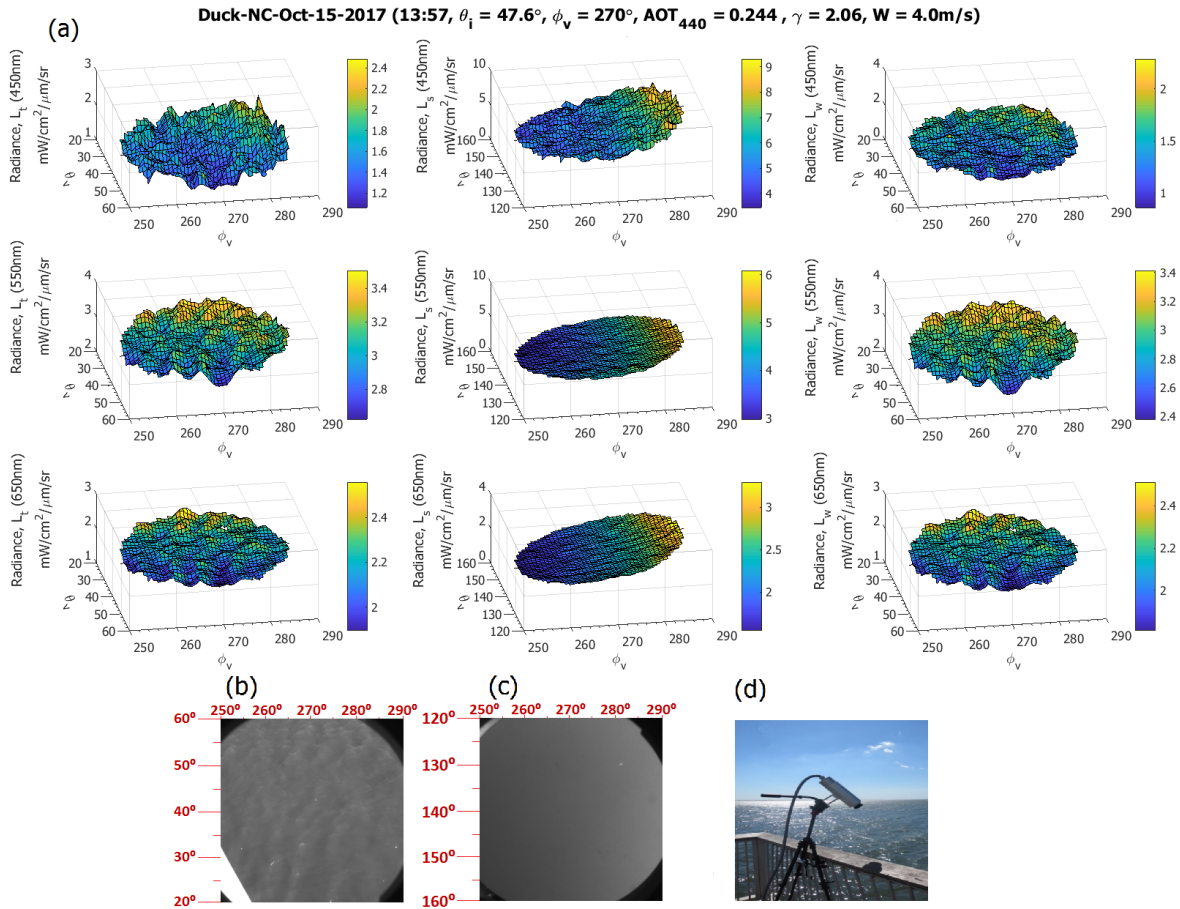


Fig. 1 a) Pixel-to-pixel variability of  $L_t$ ,  $L_s$  (left to right) for three different wavelengths: 450, 550 and 650nm (top to bottom) and  $L_w$  calculated using Eq. (2), b) corresponding panchromatic images of water surface, c) sky, and d) Snapshot hyperspectral imager in Steeplechase platform.

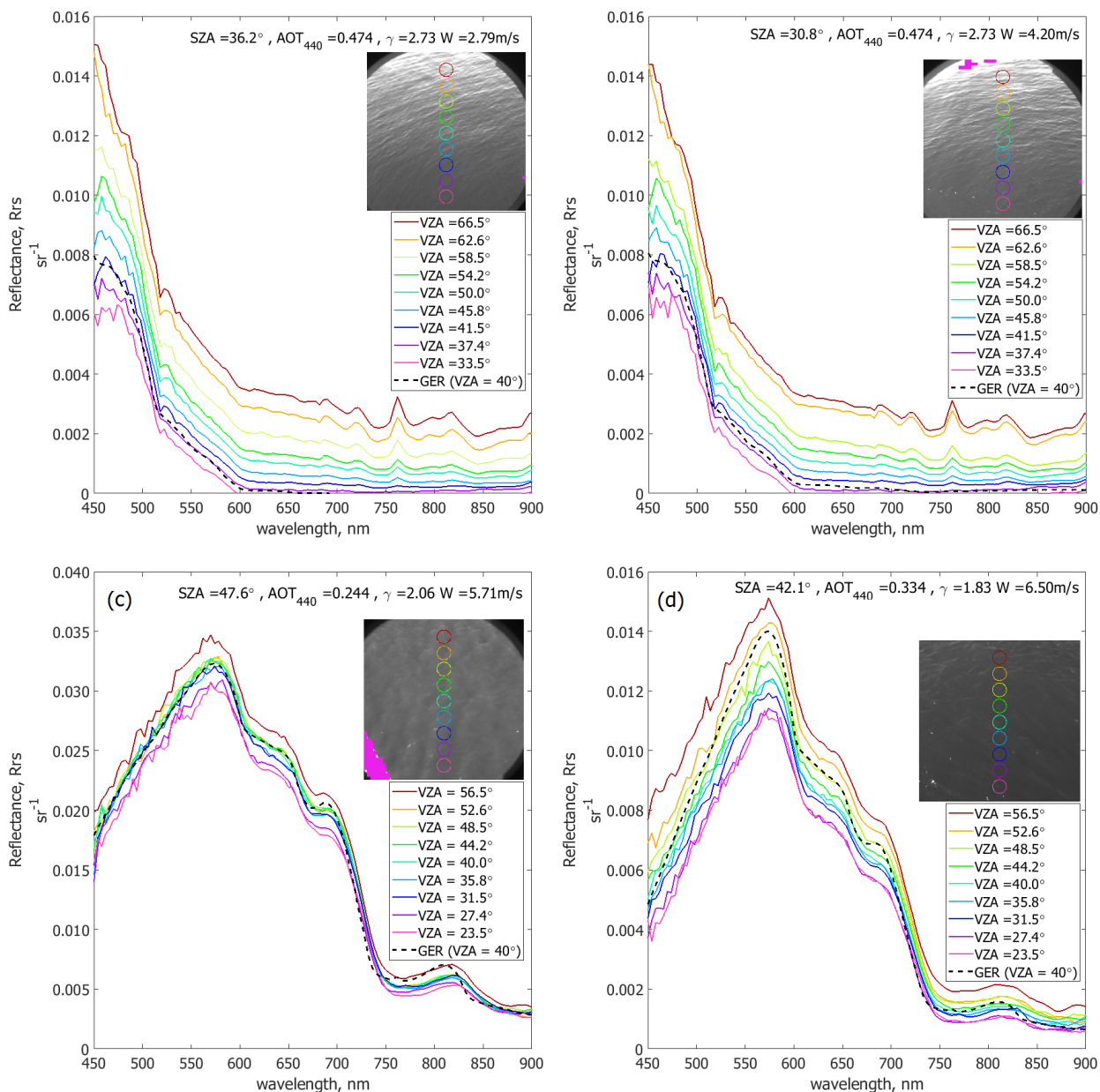


Fig. 2 Comparison of the  $R_{rs}$  from stationary and moving platforms in different water and atmospheric (SZA,  $AOT_{440nm}$ , Angstrom coefficient and wind speed are shown on inserts). a) VIIRS cruise (open ocean: Gulf of Mexico, 05/13/2017, 12:13pm), b) VIIRS cruise (open ocean: Gulf of Mexico, 05/13/2017, 12:38pm), c) DUCK pier (10/15/2017, 1:57pm), and d) Brooklyn pier (05/03/2017, 8:45am). Pixels in magenta represent saturation (mostly from Sun glint) and are excluded from all calculations.

Duck-NC-Oct-11-2017 (14:50,  $\theta_i = 51.9^\circ$ ,  $\phi_v = 90^\circ$ ,  $AOT_{440} = 0.452$ ,  $\gamma = 1.58$ ,  $W = 5.6$  m/s)

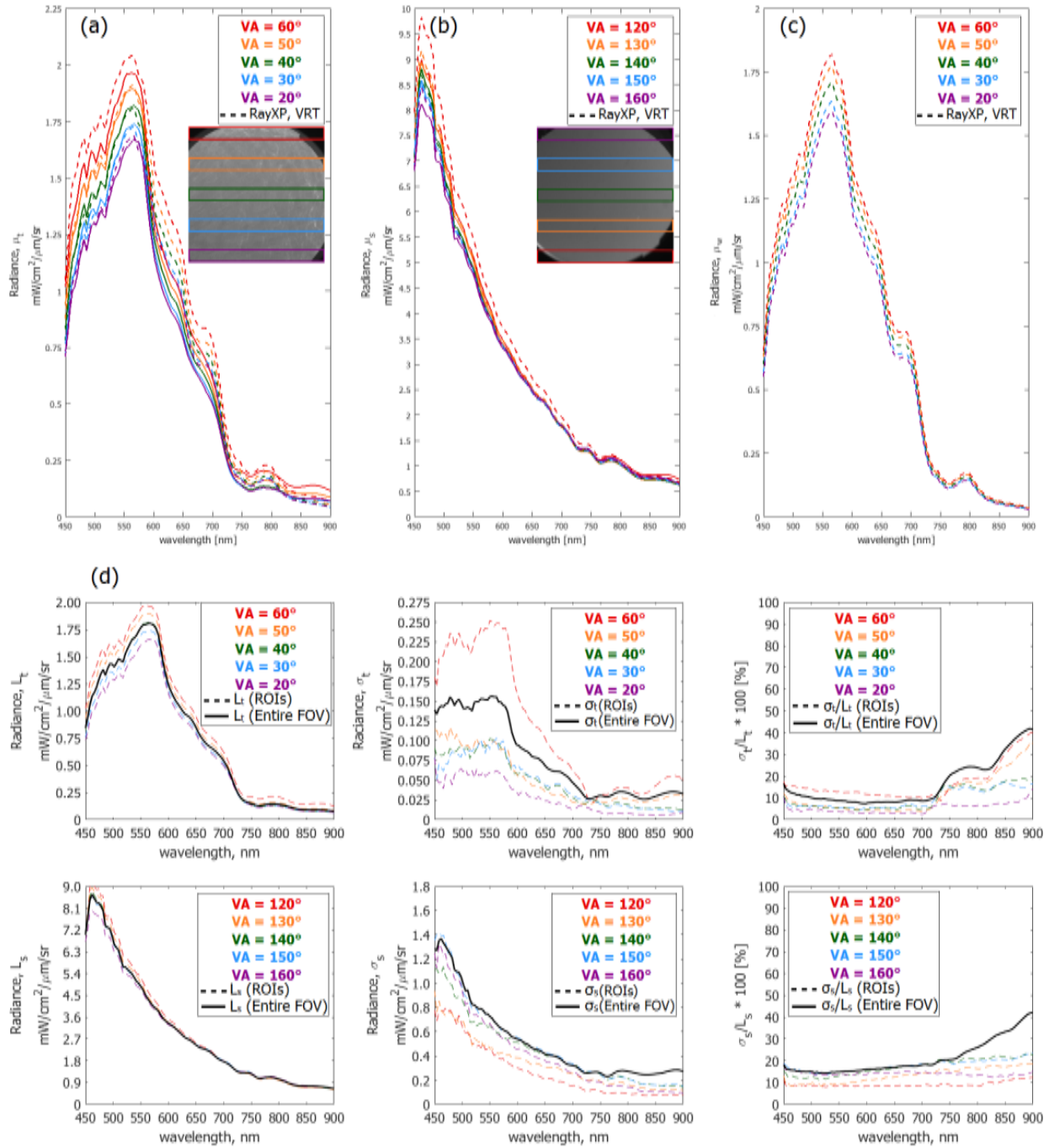


Fig. 3 Comparison of measurements and simulations for mean a)  $L_t$ , b)  $L_s$  and c) derived  $L_w$  at the FRF, 10/11/17. The insets denote the ROIs used throughout this extended abstract. Mean radiances  $L_t$  and  $L_s$ , standard deviations  $\sigma_t$  and  $\sigma_s$  for the water and sky data and corresponding ratios  $\sigma_t/L_t$  and  $\sigma_s/L_s$  for the same stations are depicted in (d) for wind speed  $W = 5.6$  m/s and different viewing angles.

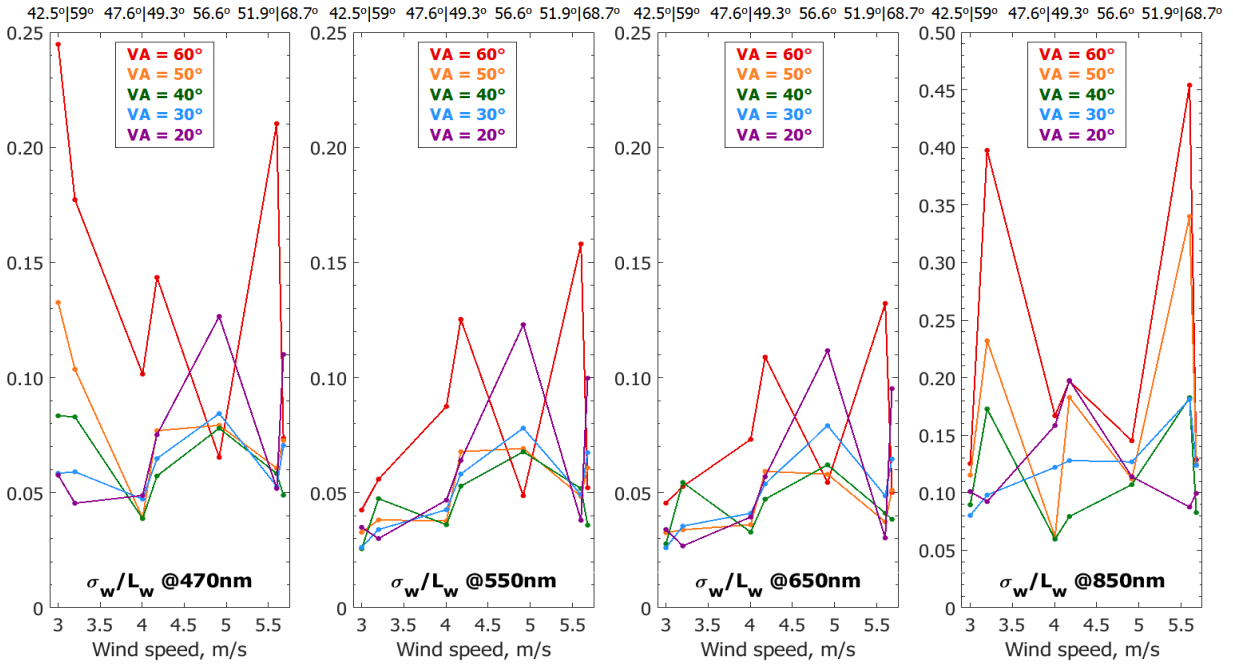


Fig. 4 The coefficient of variation for water-leaving radiance ( $\sigma_w/L_w$ ) as a function of wind speed and viewing angle: 470nm, 550nm, 650nm and 850nm (left to right).  $\sigma_w$  is determined in the assumption of constant  $\rho$  for all pixels in the same VA.

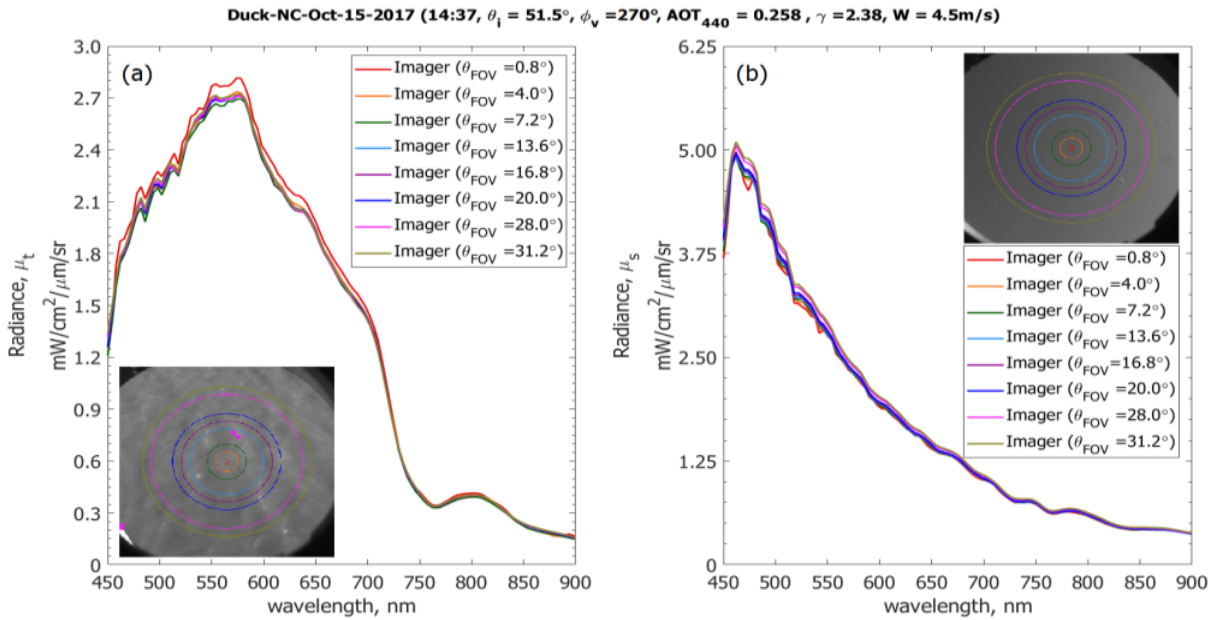


Fig. 5 (a)  $L_t$  and (b)  $L_s$  measured at  $40^\circ$  and  $140^\circ$  viewing angles as a function of FOV. The pink boxes in the image indicate saturated pixels which were excluded from the processing.

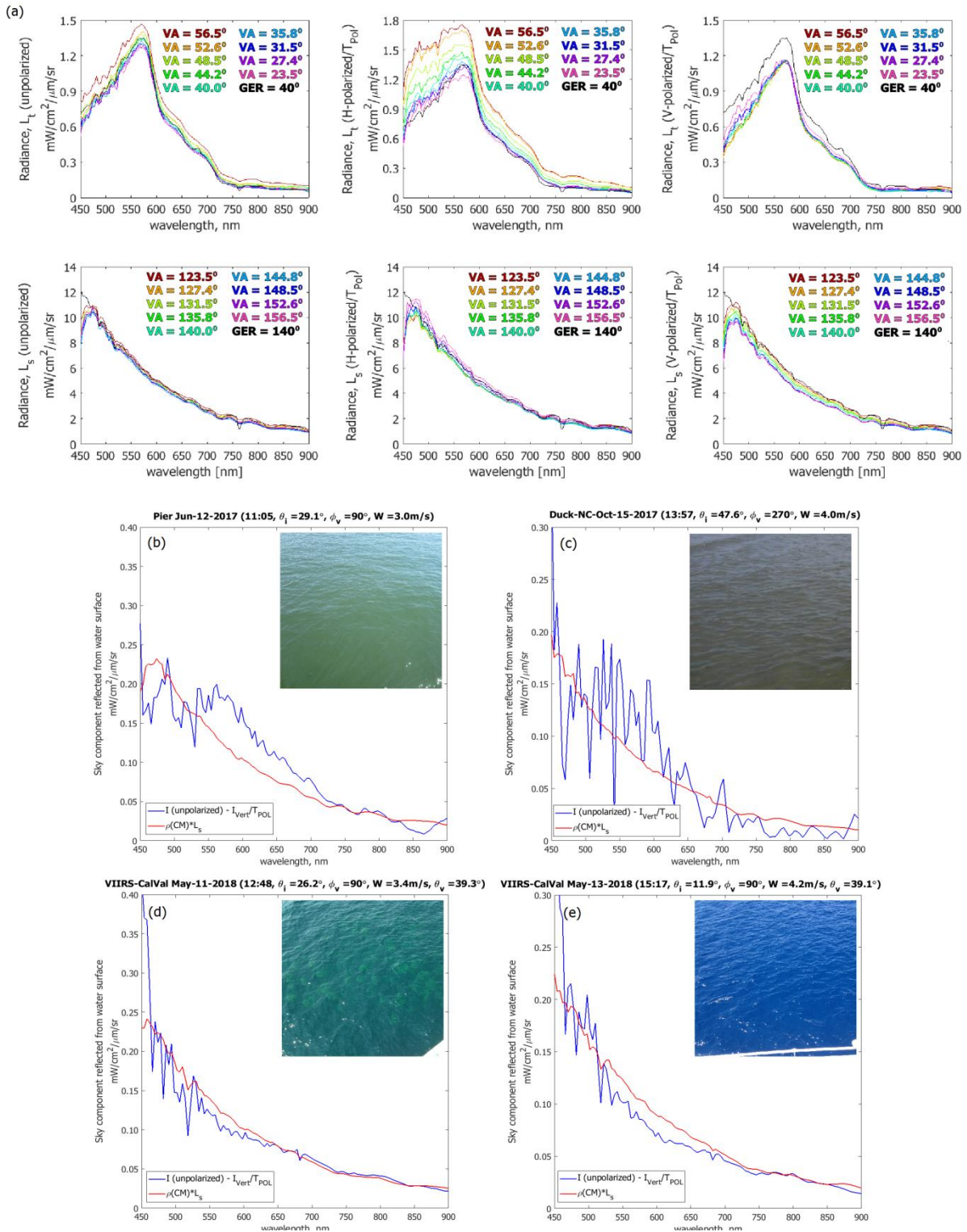


Fig. 6 Removal of sky component reflected from different water surface. a) Brooklyn pier polarized and unpolarized water and sky spectra (06/12/2017, 11:05am), b) Brooklyn pier (06/12/2017, 11:05am), c) Duck, NC pier (10/15/2017, 1:57pm), d) VIIRS cruise (coastal: Gulf of Mexico, 05/11/2017), and e) VIIRS cruise (open ocean: Gulf of Mexico, 05/13/2017).